SAND2017-10642J

Density Functional Perturbation Theory Analysis of Negative Thermal Expansion Materials: A Combined Computational and Experimental Study of α-ZrW_2O_8

Philippe F. Weck[*,†], Margaret E. Gordon[†], Charles R. Bryan[†], Jeffery A. Greathouse[†], Stephen P. Meserole[†], Mark A. Rodriguez[†], Clay Payne[†] and Eunja Kim[‡]

[†] Sandia National Laboratories, Albuquerque, New Mexico 87185, United States

[‡] Department of Physics and Astronomy, University of Nevada Las Vegas, 4505 Maryland Parkway, Las Vegas, Nevada 89124, United States

ABSTRACT: Cubic zirconium tungstate (α-ZrW_2O_8), a notorious negative thermal expansion (NTE) material, has been investigated within the framework of density functional perturbation theory (DFPT), combined with experimental characterization to assess and validate computational results. Spectroscopic, mechanical and thermodynamic properties have been derived from DFPT calculations. A systematic comparison of DFPT-simulated infrared, Raman, and phonon density-of-state spectra with Fourier transform far-/mid-infrared and Raman data collected in this study, as well as with available inelastic neutron scattering measurements, shows the superior accuracy of the PBEsol exchange-correlation functional over standard PBE calculations. The thermal evolution of the Grüneisen parameter computed within the quasi-harmonic approximation exhibits negative values below the Debye temperature, consistent with the observed NTE characteristics of α-ZrW_2O_8. The standard molar heat capacity is predicted to be $C_P^0 = 193.8$ and 192.2 J.mol^{-1}.K^{-1} with PBE and PBEsol, respectively, *ca*. 7% lower than calorimetric data. These results demonstrate the accuracy of the DFPT/PBEsol approach for studying the spectroscopic, mechanical and thermodynamic properties of materials with anomalous thermal expansion.

1. INTRODUCTION

While most solids expand upon heating as a result of anharmonic lattice dynamics,[1] negative thermal expansion (NTE) can occur in an unusual and fascinating subclass of materials that contract with increasing temperature.[2,3,4,5,6,7,8,9,10] Mechanisms underlying NTE range from structural or magnetic phase transitions to anomalous vibrational modes, such as transverse vibrational modes or rigid unit modes (RUM).[4,6,8,9] NTE has been a subject of active experimental and theoretical research for several decades, with well-documented NTE in materials such as, e.g., Si and Ge, elemental U, β-quartz, elastomers, some zeolites and ceramics with framework structures.[2,4,5,6,7,9]

Typical NTE materials exhibit anisotropic expansion, *i.e*., contraction in one or two directions coupled with positive thermal expansion in other directions, over a very limited temperature range.[4,5,6] Owing to this anisotropic expansion, microcracks affecting mechanical strength can develop in such NTE materials, leading to significant hysteresis effect in heating/cooling cycles. Although, microcracking can be used advantageously for the development of materials designed to withstand thermal shocks, isotropic NTE materials are usually preferred for most relevant technological applications.[5,6,8] Indeed, isotropic NTE materials can be used as thermal-expansion compensators in composites designed to have overall zero or adjustable thermal expansion.[8] Controlling thermal expansion of materials is of crucial importance, for example, in the production and operation of nanoscale semiconductor devices, high-precision optical systems, or high-performance thermoelectric converters and fuel cells.[5,8,9]

Very few materials, either cubic or amorphous, feature isotropic NTE over a broad temperature range, including room temperature. For example, amorphous SiO_2, CuO_2 and Si possess low-temperature isotropic NTE, and cubic AV_2O_7 (A = Zr, Hf) and AP_2O_7 (A = Th, U) exhibit isotropic NTE above room temperature.[5] Originally synthesized and characterized in the 1960's,[11,12] zirconium tungstate, ZrW_2O_8, with a relatively large and linear NTE of *ca*. -9×10^{-6} K^{-1} ranging from absolute zero up to its decomposition temperature ~1050 K, has attracted the most experimental attention among NTE materials only over the last two decades.[13,14,15,16,17,18,19,20,21,22,23,24,25,26,27,28,29] The cubic structure of ZrW_2O_8 was solved in the mid 1990's[13,14] and was initially considered to be unstable due to its tedious synthesis. The structure of low-temperature acentric α-ZrW_2O_8 phase (space group $P2_13$) is closely related to ZrV_2O_7 (space group $Pa\bar{3}$), with ZrO_6 octahedra occupying the unit-cell origin and face centers and two crystallographically distinct WO_4^{2-} tetrahedral units substituting $V_2O_7^{4+}$ groups.[13,14] Upon heating to ~431 K, α-ZrW_2O_8 transforms into the centric cubic β-ZrW_2O_8 high-temperature phase (space group $Pa\bar{3}$).[13,15,22]

Contrasting with this wealth of experimental information available on α-ZrW_2O_8, very few computational studies have been dedicated to this notorious NTE material, as recently noted by Dove and Fang.[10] Lattice dynamics simulations using classical force fields were conducted by Mittal and Chaplot in 2000,[30] and by Sanson in 2014.[31] To the best of our knowledge, the only first-principles investigations of α-ZrW_2O_8 were reported in the past few years by Ramzan et al.,[32] Gava et al.,[33] and Gupta et al.[34] Ramzan and co-

workers[32] used density functional theory (DFT), with the Perdew, Burke and Ernzerhof (PBE)[35] exchange-correlation (XC) functional, to study the high-pressure, mechanical and optical properties of α-ZrW_2O_8. Gava et al.[33] focused on predicting the mode Grüneisen parameters and NTE behavior of α-ZrW_2O_8 using DFT with the hybrid Becke three-parameter Lee-Yang-Parr (B3LYP) XC functional, according to the Debye-Einstein model of the quasiharmonic approximation (QHA). Finally, Gupta and coworkers[34] reinvestigated in more details the specific roles of anharmonic phonons responsible for the large NTE of α-ZrW_2O_8 using DFT/PBE. All aforementioned DFT studies used finite displacement methods to determine the interatomic forces and phonon frequencies needed to derive the elastic and thermal properties of α-ZrW_2O_8.

In this work, the infrared (IR), Raman, and phonon density-of-state (PDOS) spectra, mechanical and thermodynamic properties of α-ZrW_2O_8 have been extensively investigated within the framework of density functional perturbation theory (DFPT), and systematically compared with results from experimental characterization carried out in this study and previous investigations in order to assess and validate DFPT results. DFPT linear response calculations were conducted using the PBE XC functional, as in two of the previous DFT studies of α-ZrW_2O_8, as well as the revised version of PBE XC for solids (PBEsol).[36] Compared to simple finite-displacement methods typically used with DFT to determine the vibrational properties of many-particle systems, DFPT-based computational approaches can be regarded as considerably more effective, since additional physical properties (e.g., IR and Raman absorbance) can be derived from the total energy with respect to perturbations.[37] The accuracy of DFPT methods was extensively tested in previous lattice dynamics studies.[38,39,40,41,42,43]

Details of our computational approach are provided in the next section, followed by a detailed analysis and discussion of our results. A summary of our findings and conclusions is presented in the last section of the manuscript.

2. METHODS

Computational Methods. First-principles calculations were carried out using DFT, as implemented in the Vienna *ab initio* simulation package (VASP).[44] The XC energy was calculated using the generalized gradient approximation (GGA), with the PBE[35] parameterization and its PBEsol[36] revised version for solids. Both functionals were found in previous studies to correctly describe the geometric parameters and properties of a variety of Zr compounds and oxides.[38,39,40,45,46]

The interaction between valence electrons and ionic cores was described by the projector augmented wave (PAW) method.[47,48] The Zr($4p^6$,$5s^2$,$4d^2$), W($6s^2$,$5d^4$) and O($2s^2$,$2p^4$) electrons were treated explicitly as valence electrons in the Kohn-Sham (KS) equations and the remaining core electrons together with the nuclei were represented by PAW pseudopotentials. The KS equation was solved using the blocked Davidson[49] iterative matrix diagonalization scheme. The plane-wave cutoff energy for the electronic wavefunctions was set to a value of 500 eV, ensuring the total energy of the system to be converged to within 1 meV/atom. A periodic unit-cell approach was used in the total-energy relaxation calculations, with the α-ZrW_2O_8 crystal structure (space group $P2_13$, IT No. 198; Z = 4) reported by Evans *et al*.[15] utilized as the initial guess. The Brillouin zone was sampled using the Monkhorst-Pack k-point scheme,[50] with a k-point mesh of 5×5×5. No symmetry constraints were imposed in unit-cell optimization calculations. Relaxation calculations were first carried out until the Hellmann-Feynman forces acting on atoms were converged within 0.01 eV/Å.

Structures resulting from total-energy minimization with GGA/PBE and GGA/PBEsol were further relaxed with respect to Hellmann-Feynman forces until a convergence tolerance of 0.001 eV/Å was reached. Density functional perturbation theory (DFPT) linear response calculations were then carried out at these levels of theory with VASP to determine the vibrational frequencies and associated intensities. The latter were computed based on the Born effective charges (BEC) tensor, which corresponds to the change in atoms polarizabilities with respect to an external electric field. Thermal properties were further derived from phonon calculations within the QHA, which introduces a volume dependence of phonon frequencies as a part of the anharmonic effect.[51] This DFPT approach was utilized in previous computational studies to successfully predict the properties of various Zr-containing compounds and crystalline materials.[38,39,40,41,45,52,53,54,55]

Experimental Methods. All reagents were used as received for the synthesis of α-ZrW_2O_8 samples. Accurate metal concentrations in the reagents were determined via thermogravimetric analysis: heating under USP grade air to 900 °C. Following the procedure from Closmann *et al*.,[56] a 1M aqueous solution of tungsten with a volume of 50 mL and a 0.5M aqueous solution of zirconium with a volume of 50 mL were made separately from ammonium metatungstate (Aldrich) and zirconium oxychloride hydrate (Aldrich). Simultaneously, each solution was added dropwise to a stirred flask containing 25 mL deionized (DI) water. After addition, the flask was stirred for an additional 10 hours. Then, 125 mL of 6M HCl was added to the solution and mixed. The solution was placed in a Parr reactor and heated to 200 °C under autogenous pressure for 4 hours. The resulting solution was filtered and rinsed with DI water to obtain the cubic hydrated precursor $ZrW_2O_7(OH)_2(H_2O)_2$ to α-ZrW_2O_8 (see Supporting Information). The precursor was then heated to 600 °C for 10 hours, and allowed to cool to ambient temperature.

X-ray Diffraction (XRD) analysis was performed using a Bruker D2 Phaser diffractometer. This system was equipped with a sealed-tube X-ray source (Cu Kα radiation, λ = 1.5406 Å) operated at 30 kV and 10 mA. A Ni-filter was employed on the diffracted-beam side of the instrument for suppression of Kb radiation. A Lynxeye™ silicon strip detector was employed to collect the diffraction pattern with a scan rate of 15° 2θ per minute. Samples were analyzed as-received without any additional modification. XRD analysis was performed using the program JADE 9.0 (Materials Data, Inc. Livermore, CA).

Infrared spectra were collected using a Thermo Scientific Nicolet 6700 Fourier transform infrared (FT-IR) spectrometer and OMNIC 8.3 software suite, with a Spectra Tech Collector II-DRIFTS (diffuse reflectance) and an aluminum mirror as background and blank; powder was placed in holder and spectra were collected. Scans were done on the sample at a resolution of 1 cm^{-1}, with absorbance spectra ranging from 4000.12 to 649.89 cm^{-1}, using a KBr beamsplitter and a MCT/A detector. Scans were also carried out with a solid substrate beamsplitter and a DTGS-polyethylene detector using similar resolution in the range 50.14−600.23 cm^{-1}, and converted to 4.0 cm^{-1} resolution using the software.

Raman spectra were collected using a Horiba T64000 Raman Spectrometer fitted with 1800 grooves/mm gratings and a Symphony CCD detector and controlled with the LabSpec 5 software. A Coherent Verdi V10 green laser (532 nm laser at 50 mW before entering the instrument) was used for excitation. The instrument

was calibrated by analyzing a piece of silicon wafer (520.7 cm^{-1}). The α-ZrW_2O_8 spectrum shown was captured using 11 accumulations of 60 seconds from 50 to 1150 cm^{-1}. An Olympus BH2 (BHSM) microscope with a BH2-UMA fitted with a ULWD MS Plan 80 objective (NA= 0.75) was used for sampling the material. Data collection was in the single mode looking between 50 and 1150 cm^{-1}.

3. RESULTS AND DISCUSSION

Crystal Structure. Scanning electron microscope (SEM) characterization of the $ZrW_2O_7(OH)_2(H_2O)_2$ precursor and α-ZrW_2O_8 showed similar crystal habits, with elongated thin crystalline plates or filiform pointed needles (see Figure 1 below and Figures S1 and S3 in Supporting Information).

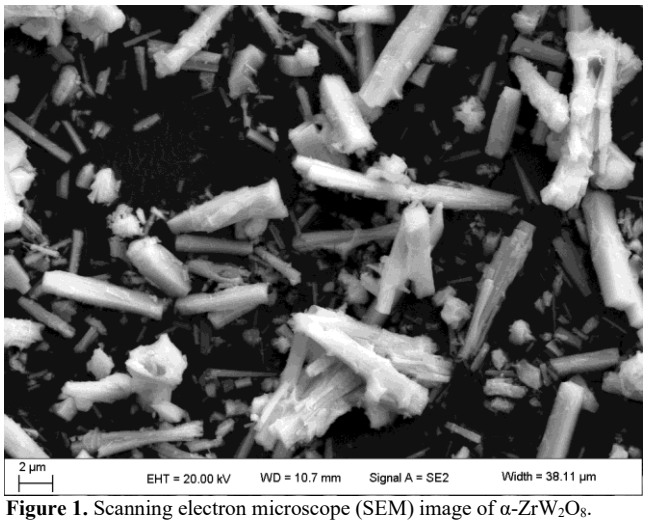

Figure 1. Scanning electron microscope (SEM) image of α-ZrW_2O_8.

Figure 2 depicts the observed X-ray diffraction pattern of α-ZrW_2O_8 (Cu Kα radiation, λ = 1.5406 Å) and simulated patterns from crystal geometries optimized with DFT at the GGA/PBE and GGA/PBEsol levels of theory, with and without relaxation of the experimental crystal lattice. The fully-relaxed structure of cubic α-ZrW_2O_8 (space group $P2_13$, IT No. 198; Z = 4) features crystal unit cell parameters of a = 9.241 Å (V = 789.10 $Å^3$) for GGA/PBEsol and a = 9.310 Å (V = 806.87 $Å^3$) for GGA/PBE at T = 0 K. These lattice parameter values in the athermal limit are ~1.0% and ~1.8% larger than the present XRD estimate of 9.1493(2) Å at T = 298 K, due to NTE in the range 0−298 K and to the fact that GGA-type functionals tend to slightly overestimate bond distances. The predicted PBEsol and PBE lattice parameters reproduce within ~0.6% and ~1.4%, respectively, the value of 9.1846(7) Å refined by Evans et al. at T = 0.3 K using a rigid unit model. As shown in Table 1, comparable agreement is obtained with previous DFT and experimental results. Let us note the superior accuracy of the lattice parameter calculated using the PBEsol XC functional over results obtained using the standard PBE functional and the hybrid B3LYP functional (see Figure 2 and Table 1). Relaxation of the unit cell lattice has only a limited impact on the simulated patterns, resulting in a small peak shift towards smaller 2θ values.

A ball-and-stick representation of the α-ZrW_2O_8 crystal unit cell is shown in Figure 3(a). As discussed in previous studies, the structure consists of corner-sharing ZrO_6 octahedral and two crystallographically distinct WO_4 tetrahedral coordination units (with metal centers labeled hereafter as W1 and W2). All atoms are positioned on 4*a* Wyckoff sites (.3. symmetry), with the exception of O1 and O2 atoms on 12*b* Wyckoff sites (1 symmetry). The bond distances calculated in this study with PBEsol and PBE, along with previous PBE and B3LYP results and XRD and neutron diffraction data are summarized in Table 1. The W1 centers possess a tetrahedral local environment with three W1−O1 bonds of 1.823 and 1.832 Å and one shorter W1−O4 bond of 1.729 and 1.732 Å with PBEsol and PBE, respectively [see Figure 3(b)]. Similarly, the local environment of the W2 centers consists of three W2−O2 bonds of 1.798 and 1.810 Å and one shorter W2−O3 bond of 1.752 and 1.755 Å with PBEsol and PBE. Octahedrally-coordinated Zr centers exibit two types of bonds, namely three Zr−O1 bonds of 2.059 and 2.077 Å and three longer Zr−O2 bonds of 2.117 and 2.130 Å predicted with PBEsol and PBE, respectively [see Figure 3(c)].

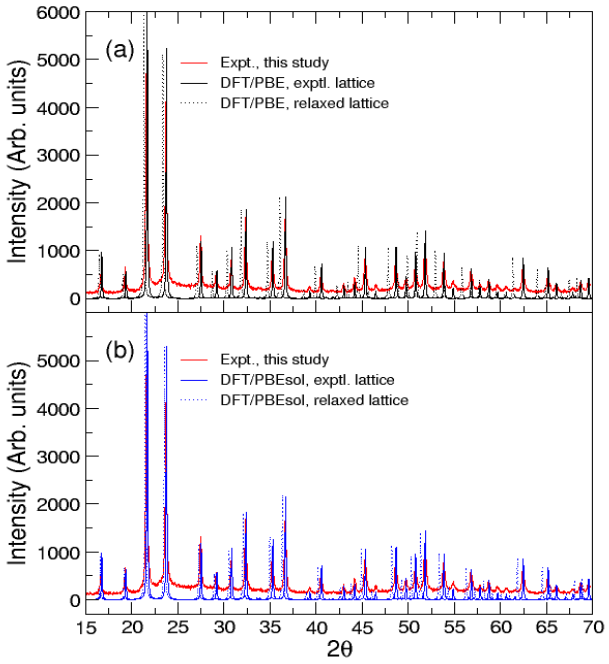

Figure 2. Observed X-ray diffraction pattern of α-ZrW_2O_8 (Cu Kα radiation, λ = 1.5406 Å) and simulated patterns from crystal geometries optimized with DFT at the (a) GGA/PBE and (b) GGA/PBEsol levels of theory, with and without relaxation of the experimental crystal lattice.

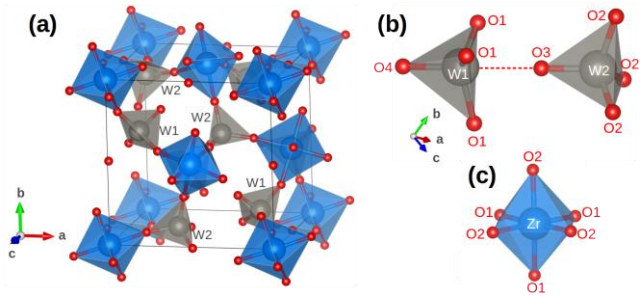

Figure 3. (a) Crystal unit cell of α-ZrW_2O_8 (space group $P2_13$, IT No. 198; Z = 4), with corner-sharing ZrO_6 octahedral (blue) and WO_4 tetrahedral (grey) coordination units; (b) Relative arrangement of the two crystallographically distinct WO_4 tetrahedra along the threefold symmetry axis (dashed line); (c) ZrO_6 coordination octahedron.

As shown in Table 1, the best agreement between DFT results and the low-temperature (T = 0.3 K) bond distances measured by Evans et al. is obtained using the PBEsol functional, followed by PBE and B3LYP functionals.

Table 1. Crystal Structure Properties (in Å) of α-ZrW_2O_8 (Space Group $P2_13$, IT No. 198; Z = 4) Calculated with Density Functional Theory and Measured Using X-Ray and Neutron Diffraction.

	T(K)	a	Zr−O1	Zr−O2	W1−O1	W1−O4	W2−O2	W2−O3
PBEsol [a]	0	9.241	2.059	2.117	1.823	1.729	1.798	1.752
PBE [a]	0	9.310	2.077	2.130	1.832	1.732	1.810	1.755
PBE [b]	0	9.320	2.077	2.137	1.835	1.732	1.810	1.756
B3LYP [c]	0	9.352	2.065	2.147	1.846	1.749	1.813	1.779
Expt.[a]	298	9.1493(2)	1.93(3)	2.17(3)	1.97(3)	1.51(4)	1.78(3)	1.71(3)
Expt.[d]	293	9.15993(5)	2.0420	2.1085	1.7975	1.7071	1.7819	1.7325
Expt.[e]	293	9.1575(2)	2.0397	2.1169	1.8011	1.7241	1.7713	1.6940
Expt.[e]	0.3	9.1846(7)	2.0393	2.1131	1.8276	1.739	1.7793	1.714

[a]This study. [b]Gupta et al., 2013; ref 34. [c]Gava et al., 2012; ref 33. [d]Mary et al., 1996; ref 13 . [e]Evans et al., 1996; ref 15.

The PBE bond distances computed in this study are in line with those reported by Gupta et al.[34] at the same level of theory. The bond distances refined from XRD analysis at T = 298 K in this study are overall consistent with previous combined XRD/neutron diffraction structural models by Mary et al.[13] and Evans et al.[15] at T = 293 K.

Phonon, Infrared, and Raman Spectroscopic Properties. DFPT was used at the GGA/PBE and GGA/PBEsol levels of theory to calculate the forces exerted on atoms of the equilibrium structure of bulk α-ZrW_2O_8 and phonon frequencies were computed at the center of the Brillouin zone (Γ-point). Figure 4 shows the resulting phonon density-of-states spectra simulated at T = 0 K, along with generalized PDOS spectrum from inelastic neutron scattering data collected at T = 300 K using time-of-flight (TOF) and filter-analyser (FA) spectroscopy to probe the low and high phonon-energy range, respectively.[18] Overall, good agreement is obtained between DFPT predictions and experiments, with the notable exception of phonon signatures observed in the vicinity of $\omega \cong 600$ cm^{-1}, which are not reproduced by calculations. Phonon frequencies calculated with PBEsol appear systematically blueshifted compared to PBE results, with larger differences occurring above $\omega \cong 350$ cm^{-1}.

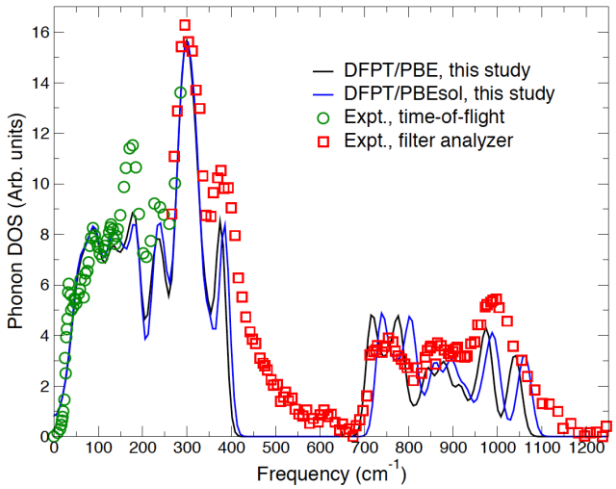

Figure 4. Phonon density-of-states (PDOS) spectra of α-ZrW_2O_8 simulated at T = 0 K using density functional perturbation theory (DFPT) at the GGA/PBE (black line) and GGA/PBEsol (blue line) levels. The generalized PDOS spectrum from inelastic neutron scattering data collected at T = 300 K using time-of-flight (TOF; green circles) and filter-analyser (FA; red squares) spectroscopy [Ref. (18)] is shown for comparison. A smearing width of σ = 10 cm^{-1} was used to generate PDOS spectra.

With four formula units per unit cell (i.e., N = 44 atoms), α-ZrW_2O_8 possesses $3N$ = 132 degrees of freedom, which are distributed among 55 phonons, namely, 54 optical phonons ($\Gamma_{optical}$) and one acoustic phonon ($\Gamma_{acoustic}$). The latter corresponds to triply-degenerate modes of translation at the Γ-point, *i.e.*, one longitudinal acoustic mode and two transverse acoustic modes with zero-frequency, and is associated with the T irreducible representation [irrep; $\Gamma_{acoustic}(3) = T$] of the cubic point group[57] for α-ZrW_2O_8 (cf. Table 2). The remaining 129 optical modes can be represented as $\Gamma_{optical}(129) = 11A + 11E + 32T$, where vibrational modes belonging to the T, E and A irreps are triply-, doubly- and non-degenerate, respectively. Optical phonons can be further separated into subgroups as follows: $\Gamma_{optical}(129) = \Gamma_{lattice}(9) + \Gamma_{trans}(24) + \Gamma_{libr}(24) + \Gamma_{int}(72)$, where $\Gamma_{lattice}(9) = A + E + 2T$ are lattice modes associated with the motion of Zr atoms, $\Gamma_{trans}(24) = 2A + 2E + 6T$ and $\Gamma_{libr}(24) = 2A + 2E + 6T$ correspond to WO_4 modes of translation and libration (*i.e.*, hindered rotation), and $\Gamma_{int}(72) = 6A + 6E + 18T$ are distorted WO_4 unit internal modes of vibration. Using a correlation diagram, a direct correspondence can be established between the internal modes of WO_4 units in the α-ZrW_2O_8 crystal and a free tungstate ion, which features symmetric (ν_1) and antisymmetric (ν_3) stretching modes, as well as symmetric (ν_2) and antisymmetric (ν_4) bending modes.[58,59] The 72 internal modes of WO_4 units can be subdivided into the following four categories: $\upsilon_1 \rightarrow 2A + 2T$, $\upsilon_2 \rightarrow 2E + 4T$, $\upsilon_3 \rightarrow 2A + 2E + 6T$, and $\upsilon_4 \rightarrow 2A + 2E + 6T$. A full assignment of the 55 phonons calculated with DFPT at the PBE and PBEsol levels is reported in Table 3. PBEsol (PBE) calculations predict symmetric ν_1 stretching modes in the range 1013−1032 cm^{-1} (993−1012 cm^{-1}), antisymmetric ν_3 stretching modes in the range 739−992 cm^{-1} (717−975 cm^{-1}), antisymmetric ν_4 and symmetric ν_2 bending modes in the range 277−381 cm^{-1} (276−374 cm^{-1}), and a combination of libration, lattice and translation modes below 256 cm^{-1} (253 cm^{-1}). Large gaps of 358 cm^{-1} and 343 cm^{-1} computed with PBEsol and PBE, respectively, separate the high-frequency stretching modes from the low-frequency bending modes. These findings are consistent with the 318 cm^{-1} wide gap between 416 and 734 cm^{-1} recently calculated by Gava et al.[33] using DFT with the B3LYP hybrid functional, although spectral signatures were observed in this range in the generalized PDOS spectrum from inelastic neutron scattering data collected at T = 300 K.[18]

Table 2. Character Table for α-ZrW_2O_8 (Space Group $P2_13$, IT No. 198; Cubic Point Group T(23); See ref. 57).

Irrep.[a]	Multiplicity	E	$3C_2$	$4C_3$	$4(C_3)^2$	Functions/Rotations
T	33	3	-1	0	0	(x,y,z) (xy,yz,xz) (R_x,R_y,R_z)
E	11	2	2	-1	-1	$(x^2\text{-}y^2, 3z^2\text{-}r^2)$
A	11	1	1	1	1	$x^2+y^2+z^2$

[a]Vibrational modes belonging to the T, E and A irreducible representations (irrep.) are triply-, doubly- and non-degenerate, respectively.

Table 3. Vibrational Eigenfrequencies for α-ZrW_2O_8 (space group $P2_13$, IT No. 198) Calculated from Density Functional Perturbation Theory (DFPT) at the GGA/PBE and GGA/PBEsol Levels. Observed IR- and Raman-Active Bands Are Reported for Comparison.

Irrep.[a]	DFPT (cm^{-1})		IR (cm^{-1})		Raman (cm^{-1})			Mode Description[e]
	PBE[b]	PBEsol[b]	Expt.[b]	Expt.[c]	Expt.[b]	Expt.[c]	Expt.[d]	
A	1012	1032			1030	1028_m	1034	↑
T	1004	1021			1020		1021	
A	1003	1019						$\nu_1(WO_4)$
T	993	1013					987	↓
T	975	992	998	999_w	969	966_w	970	↑
A	915	919			931	929_m	933	
T	888	900	908	907_m	903	901_m	907	
T	850	861	873	871_s		887_w	890	
A	843	855				859_w	863	$\nu_3(WO_4)$
T	771	798	799	800_s			807	
E	769	796			792	789_s	794	
T	732	756	760	760_m			747	
E	721	744			737	733_m	737	
T	717	739	734	739_m			725	↓
T	374	381	399					↑
E	369	377			383	382_w	382	
T	367	375	393					
T	347	352	368				350	
A	342	346						
T	325	325						
E	320	323			332	331_m	331	
T	320	321	332					
T	307	307	321					$\nu_4(WO_4)$
E	299	300			309	308_w	307	+
T	297	299						$\nu_2(WO_4)$
T	291	295	305				298	
T	290	292						
A	283	286						
T	283	284	292					
E	276	277				271	270	↓
T	253	256	262				243	↑
E	234	238			235	234_w	236	
T	234	237	240					
A	233	236						
T	225	228	222					
A	201	197					205	
T	187	190	193		181		181	
T	176	177	185					
T	172	172	174					
E	169	171					170	
T	157	152	161					
E	142	140			143	144_m	143	
T	128	128	132					
A	125	123						Libration + Lattice +
T	100	97	97					Translation
E	94	93			104	103_w	113	
T	82	91	86		77	84_w	91	
A	74	73			66	65_m	69	
T	68	72	78					
T	60	64	71					
T	60	59						
A	51	48					50	
E	42	37				40_m	41	
T	39	36						↓
T	0	0						Acoustic

[a]Vibrational modes belonging to the *T*, *E* and *A* representations are Raman active (quadratic functions), while only *T* modes are IR active (linear functions). [b]This study. [c]Evans et al., 1996; ref 15; Band intensity: s = strong m = medium, w = weak. [d]Ravindran et al., 2001; ref 24. [e] Free tungstate ion vibration modes: symmetric (ν_1) and antisymmetric (ν_3) stretching modes, symmetric (ν_2) and antisymmetric (ν_4) bending modes.

Eigenfrequencies predicted with DFPT have also been systematically compared to IR and Raman bands observed in this study and in previous experiments by Evans et al.[15] and Ravindran et al.[24] (cf. Table 3). As shown in Table 2, all the optical modes belonging to the *T*, *E* and *A* irreps are Raman active (quadratic functions), while only optical modes from the *T* irrep are IR active (linear functions).

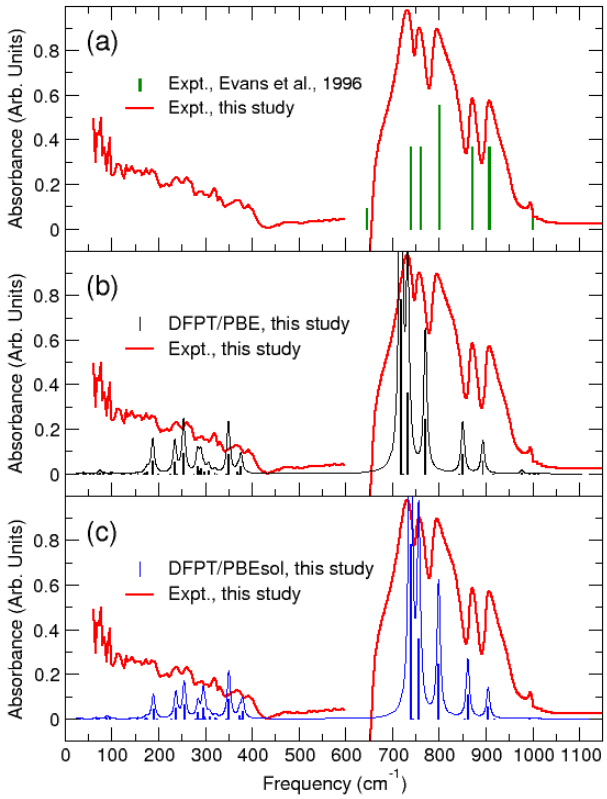

Figure 5. (a) Fourier transform infrared (FT-IR) spectrum of α-ZrW_2O_8 measured in this study at $T = 298$ K (red line) and observed IR band centers reported by Evans *et al.* [Ref. (15)] (green peaks), along with infrared spectra simulated from density functional perturbation theory (DFPT) at the (b) GGA/PBE (black line/peaks) and (c) GGA/PBEsol (blue line/peaks) levels. Natural line broadening was simulated from DFPT eigenfrequencies using a Lorentzian lineshape function with a full width at half maximum (FWHM) of 4 cm^{-1}.

As shown in Table 3 and Figure 5, the FT-IR bands observed by Evans et al.[15] at 999 cm^{-1} (*w*: weak), 907 cm^{-1} (*m*: medium), 871 cm^{-1} (*s*: strong), 800 cm^{-1} (*s*), 760 cm^{-1} (*m*) and 739 cm^{-1} (*m*) are well reproduced by the FT-IR spectrum collected in this study. The IR spectrum simulated using PBEsol is in closer agreement with experiments over this frequency range than that predicted with PBE. The IR-active frequencies observed by Evans et al.[15] at 646 cm^{-1} (*w*) and in the range 600-400 cm^{-1} (*w*) were not predicted by DFPT calculations, nor observed in the present experiments. This discrepancy is similar to the one mentioned above in the comparison between the generalized PDOS spectrum from inelastic neutron scattering data and PDOS simulated with DFPT. Based on previous FT-IR investigations,[60,61] it can be inferred these additional IR bands observed by Evans et al.[15] originate from the formation of ZrO_2 and WO_3, which are thermodynamically more stable around room temperature than the α-ZrW_2O_8 compound.[62]

Using combined FT-IR measurements and DFPT calculations, new and extensive assignments were made for the far-infrared (<400 cm^{-1}) spectrum of α-ZrW_2O_8. As show in Table 3, seven IR-active bands corresponding to $\nu_4(WO_4)$ and $\nu_2(WO_4)$ were found in the FT-IR spectrum observed between 399 and 292 cm^{-1}, in addition to twelve IR bands assigned as libration, lattice and translation modes between 262 and 71 cm^{-1}. The lowest-frequency IR-active mode predicted at 36 and 39 cm^{-1} with PBEsol and PBE, respectively, could not be observed in FT-IR experiments.

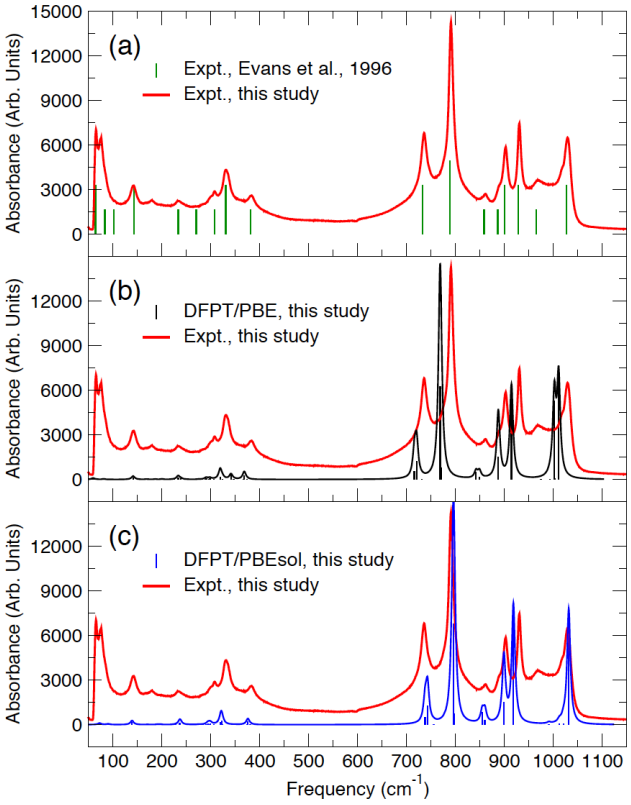

Figure 6. Raman spectrum of α-ZrW_2O_8 measured in this study at $T = 298$ K (red line) and observed Raman band centers reported by Evans *et al*. [Ref. (15)] (green peaks), along with Raman spectra simulated from density functional perturbation theory (DFPT) at the (b) GGA/PBE (black line/peaks) and (c) GGA/PBEsol (blue line/peaks) levels. Natural line broadening was simulated from DFPT eigenfrequencies using a Lorentzian lineshape function with a full width at half maximum (FWHM) of 4 cm^{-1}.

The Raman spectra simulated with DFPT at the PBEsol and PBE levels, along with the Raman-active bands observed at room temperature in this study and by Evans et al.[15] are shown in Figure 6, with the corresponding vibrational eigenfrequencies listed in Table 3, which also includes Raman band centers measured by Ravindran et al.[24] at $T = 20$ K. All three sets of observed Raman bands appear to be consistent overall, although a larger number of Raman-active bands was reported by Ravindran et al.[24] Instead of the fourteen Raman bands expected above 600 cm^{-1} from group theory analysis (cf. Table 3), twenty bands were observed by Ravindran et al.[24] Comparison between their Raman results and PBEsol predictions show that the band observed at 1021 cm^{-1} (1020 cm^{-1} in this study) is actually a combination of two bands predicted at 1021 cm^{-1} (*T* irrep) and 1019 cm^{-1} (*A* irrep). In addition, the bands centers observed Ravindran et al.[24] at 855, 841, 779, 718, 685, 645 and 628 cm^{-1} do not appear to coincide with any of the α-ZrW_2O_8 Raman bands predicted with DFPT or measured in this study or by Evans et al.[15] or by Perottoni and da Jornada.[20] As aforementioned, some of these Raman bands might stem from the formation of stable ZrO_2 and WO_3 products at room temperature. Let us note that, similar to PDOS and IR DFPT calculations, no Raman active modes

are predicted to occur in the ranges 381-739 cm^{-1} and 374-717 cm^{-1} with PBEsol and PBE, respectively.

Thermodynamic Properties. Phonon calculations near equilibrium were carried out within the QHA to obtain the thermal properties of α-ZrW_2O_8 at constant pressure. A volume dependence of phonon frequencies is introduced within the QHA as a part of anharmonic effect.[51] A temperature effect was added to the total energy $U(V)$ of the system through the phonon contribution, F_{phonon}, calculated at constant volume as a function of the temperature T according to:

$$F_{phonon}(T) = \frac{1}{2}\sum_{\mathbf{q},v}\hbar\omega_{\mathbf{q},v} + k_B T \sum_{\mathbf{q},v}\ln\left[1 - e^{-\beta\hbar\omega_{\mathbf{q},v}}\right], \quad (1)$$

where $\mathbf{q}$ and v are the wave vector and band index, $\hbar$ is the reduced Planck constant, $\hbar\omega_{\mathbf{q},v}$ is the energy of a single phonon with angular frequency $\omega_{\mathbf{q},v}$, k_B is the Boltzmann constant, T is the temperature of the system, and $\beta = (k_B T)^{-1}$. Figure 7 depicts the variation of the $U(V) + F_{phonon}(T;V)$ energy of α-ZrW_2O_8 with the unit-cell volume computed with DFPT at the PBE and PBEsol levels, in the temperature range T = 0−450 K. While qualitatively similar, the variation of the locus of points corresponding to the local minimum of each free energy curve (red diamonds in Figure 7) appears more pronounced for PBEsol than for its PBE counterpart.

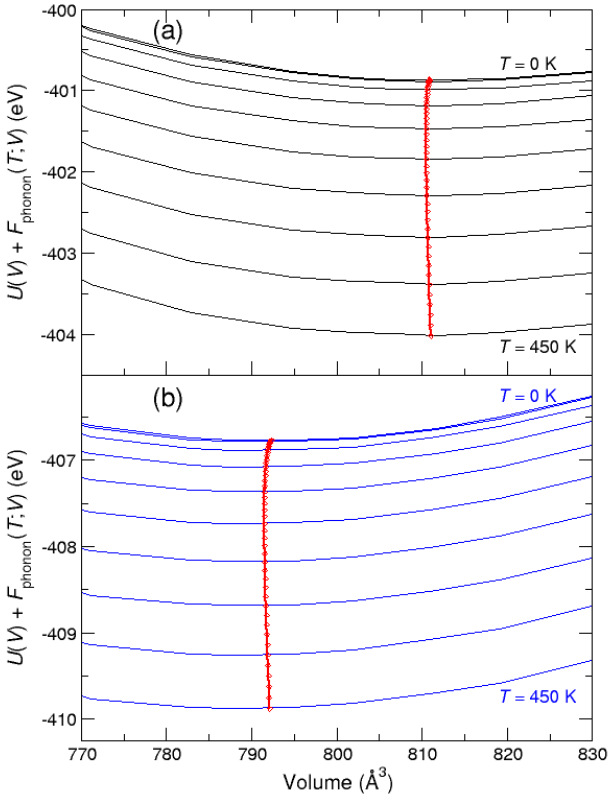

Figure 7. Variation of the total energy with phonon contribution, $U(V)+F_{phonon}(T;V)$, of α-ZrW_2O_8 as a function of the unit-cell volume computed with density functional perturbation theory at the (a) GGA/PBE and (b) GGA/PBEsol levels from T = 0 K to 450 K, by step of 50 K. The local minimum of each free energy curve, by step of 10 K, is indicated by a red diamond.

In order to determine the thermal properties of α-ZrW_2O_8 at constant pressure, a volume dependence of the thermodynamic functions is introduced through a transformation. The Gibbs free energy is defined at constant pressure by the following transformation:

$$G(T,P) = \min_V\left[U(V) + F_{phonon}(T;V) + PV\right], \quad (2)$$

where $\min_V$ [function of V] corresponds to a unique minimum of the expression between brackets with respect to the volume V, U is the total energy of the system, and P is the pressure. $U(V)$ and $F_{phonon}(T;V)$ were calculated and the thermodynamic functions of the right-hand side of the equation above were fitted to the integral form of the Vinet equation of state (EoS). The universal Vinet[63] EoS is expressed as:

$$P(V) = 3K_0\frac{(1-x)}{x^2}\exp\left[\frac{3}{2}(K_0' - 1)(1-x)\right], \quad (3)$$

where P is the uniform hydrostatic pressure, V_0 is the reference volume, V is the deformed volume, and the bulk modulus and its first derivative with respect to the pressure are given by

$$K_0(T) = -V\left(\frac{\partial P}{\partial V}\right)_{P=0} \text{ and } \quad K_0'(T) = \left(\frac{\partial K}{\partial P}\right)_{P=0} \quad (4)$$

and where

$$x = \left(\frac{V}{V_0}\right)^{\frac{1}{3}}. \quad (5)$$

Table 4. Elastic Constants (C_{ij}) of α-ZrW_2O_8 Calculated at T = 0 K at the PBEsol and PBE Levels and Bulk (K), Shear (G), and Young's (E) Moduli, Poisson's Ratio (v), and Debye Temperature (θ_D) Derived within the Voigt-Reuss-Hill Approximation. Previous Calculations and Experimental Estimates Are Also Reported.

method	C_{11}	C_{12}	C_{44}	K	G	E	v	θ_D
PBEsol[a]	162.8	77.2	29.8	105.7	34.4	93.2	0.353	337
PBE[a]	154.3	70.9	31.0	98.7	34.9	93.8	0.342	341
PBE[b]	137.6	66.7	24.9	90.3				
PBE[c]	144.8	65.6	22.6	92.0	29.4	79.7	0.356	314
LDA[c]	157.7	78.7	30.5	105.0	34.1	92.3	0.354	335
Exptl.[d]	161.8	75.5	29.4	104.3	36.8	98.8	0.342	333

[a]This study. [b]Gupta et al., 2013; ref 34. [c]Ramzan et al., 2011; ref 32. [d]Drymiotis et al., 2004; ref 25; resonant-ultrasound spectroscopy at T = 0K.

In the zero-temperature limit, the bulk modulus values for single-crystal α-ZrW_2O_8 computed using the Vinet EoS are K_0 = 90.2 and 96.7 GPa ($K_0' = 4.2$ and 3.4) with the PBE and PBEsol functionals, respectively, in agreement with the experimental value of 104.3 GPa obtained by resonant-ultrasound spectroscopy near T = 0 K.[25] These computed bulk moduli are also consistent with the Voigt-Reuss-Hill (VRH) estimates of 98.7 GPa for PBE and 105.7 GPa for PBEsol derived from the elastic constants calculated at T = 0 K with DFPT as the second derivatives of the energy with respect to the strain (cf. Supporting Information). As shown in Table 4, elastic constants calculated with PBEsol, i.e., $C_{11} = 162.8$ GPa, $C_{12} = 77.2$ GPa, and $C_{44} = 29.8$ GPa, are in closer agreement with the resonant-ultrasound data of $C_{11} = 161.8$ GPa, $C_{12} = 75.5$ GPa, and $C_{44} = 29.4$ GPa measured by Drymiotis et al.[25] than PBE and LDA predictions. The Born stability conditions[64,65] are satisfied by both calculated and measured elastic constants, thus indicating mechanical stability of α-ZrW_2O_8 (see Supporting Information). The shear (G) and Young's (E) moduli, Poisson's ratio (v), and Debye temperature (θ_D) were also derived from elastic constants and compared to available experimental data (cf. Table 4 and Supporting Information).

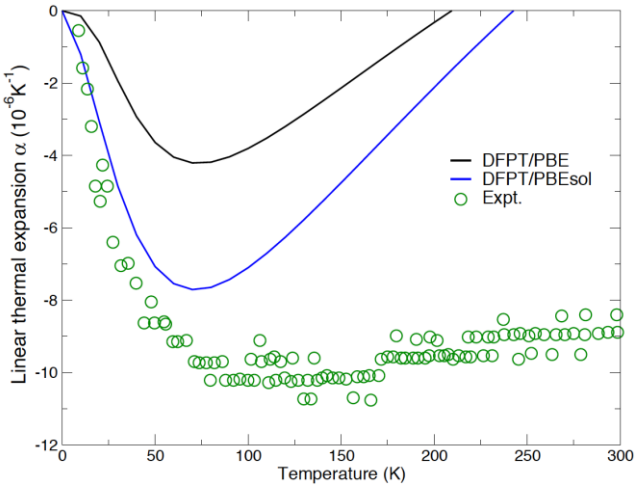

Figure 8. Linear coefficient of thermal expansion (CTE) of α-ZrW_2O_8 single crystal computed with density functional perturbation theory (DFPT) at the GGA/PBE and GGA/PBEsol level**s** within the quasi-harmonic approximation. Experimental linear CTE estimates (green circles) extracted from the high-resolution neutron diffraction data for polycrystalline ZrW_2O_8 (Ref. 19) are represented for comparison.

As shown in Figure 7, the volume dependence of the phonon free energy changes as a function of temperature, associated with a temperature-dependent equilibrium volume of α-ZrW_2O_8. Within the QHA approach, this volume variation can be assimilated to thermal expansion. The variations of the linear coefficient of thermal expansion (CTE), $\alpha_L(T)$, of α-ZrW_2O_8 predicted with DFPT at the GGA/PBE and GGA/PBEsol level**s** are depicted in Figure 8, along with experimental linear CTE estimates extracted from the high-resolution neutron diffraction data of David *et al*.[19,24] As mentioned in previous studies,[15] the linear CTE is usually calculated assuming isotropic expansion/contraction with the expression $\alpha_L = a_0^{-1}\,\Delta a/\Delta T$, where the reference lattice parameter a_0 ($a = V^{1/3}$) corresponds here to a temperature of T = 0 K and $\Delta a/\Delta T$ is the variation of the lattice parameter with temperature. The linear CTE initially obtained from neutron diffraction data collected by Evans *et al*.[15] for a polycrystalline sample was -8.7×10^{-6} K^{-1} ($T = 0.3 - 693$ K), with a lattice parameter dependence of the form $a(T) = a_0 + a_1T^2 + a_2Te^{-a_3/T}$.[66] The value subsequently measured by Ernst *et al*.[18] using neutron Bragg diffraction from a single crystal of α-ZrW_2O_8 was $-9.39 \pm 0.03 \times 10^{-6}$ K^{-1} above 50 K. The latest high-resolution neutron diffraction data of David *et al*. [19] for polycrystalline ZrW_2O_8 yielded a value of -9.54×10^{-6} K^{-1} at 520 K, with a reference at 2 K. Grüneisen's vibrational theory of thermal expansion was used to calculate the PBEsol and PBE linear CTE displayed in Figure 8.[67,68] Within this approach, the thermal expansion of isotropic materials such as α-ZrW_2O_8 can be expressed as $\alpha_L = \sum_i \alpha_i = \gamma C_V/3K$, where K and C_V are the bulk modulus and the specific (isochoric) heat capacity, respectively, and the mean Grüneisen parameter γ can be decomposed into as $\gamma = \sum_i \gamma_i c_i \,/\, \sum_i c_i$, where the mode Grüneisen parameters $\gamma_i = -\partial \ln \omega_i \,/\, \partial \ln V$ represent the relative change of mode frequencies ω_i with the unit-cell volume V and c_i are the contributions of these vibrational modes to the total specific heat C_V. As shown in Figure 8, the negative thermal expansion computed using PBEsol is in very good agreement with experimental data up to ~70 K, where it reaches an extremum of -7.7×10^{-6} K^{-1}. Predictions using PBE are qualitatively similar to PBEsol, although the maximum NTE value predicted is only -4.2×10^{-6} K^{-1} at ~70 K. Above this temperature, both PBEsol and PBE results exhibit smaller NTE values and, eventually, positive thermal expansion is predicted above 209 K and 243 K with PBE and PBEsol, respectively. While reduction in NTE also appears above ~70 K in the experimental data of David et al.[19,24] for polycrystalline ZrW_2O_8, computational predictions for single crystal α-ZrW_2O_8 are markedly different from measurements, which oscillate between -10.8×10^{-6} K^{-1} and -8.4×10^{-6} K^{-1} in the temperature range ~70–300 K. Discrepancies between finite-displacement DFT calculations with the B3LYP hybrid functional and experimental thermal expansion data above ~60 K were also found by Gava et al.[33] These differences were attributed to the creation of thermally induced defects in real α-ZrW_2O_8 samples, as precursors to the thermally activated $\alpha \rightarrow \beta$ phase transition in cubic ZrW_2O_8, which occurs around 431 K.[13,15,22] Such low-temperature defect creation scenario is plausible owing to the metastable character of α-ZrW_2O_8, which is only thermodynamically stable in a narrow temperature range around 1400 K.[62]

Since both the bulk modulus and the specific heat are positive in the expression of the thermal expansion $\alpha_L = \gamma C_V/3K$, the Grüneisen parameter γ is the pivotal parameter dictating positive or negative thermal expansion, with NTE originating from vibrational modes with $\gamma_i < 0$. The thermal evolution of the Grüneisen parameter of α-ZrW_2O_8 calculated using DFPT at the GGA/PBE and GGA/PBEsol levels within the QHA is depicted in Figure 9, along with the experimentally derived Grüneisen parameter reported by Ernst and co-workers.[18] Results obtained using PBEsol are in excellent agreement with experimental estimates to ~60 K, while PBE predictions systematically underestimate experimental data. Calculations at the PBEsol and PBE levels indicate that γ is negative below 245 and 210 K, respectively, with minima of -6.56 at 10 K for PBEsol and -1.11 at 30 K for PBE and that γ remains close to zero up to 450 K. This finding is consistent with the observation by David et al.[19] that phonon modes have little net effect on the lattice expansion between ~300-550 K. The main contributions to NTE at low temperature stem from the two lowest-frequency optical phonons, predicted at 36 cm^{-1} (T irrep) and 37 cm^{-1} (E irrep) with PBEsol and at 39 and 42 cm^{-1} with PBE. These results are in line with previous calculations carried out within the Debye-Einstein QHA showing that both vibrational modes accounts for up to ~70% of the CTE in the vicinity of 30 K.[33] These modes are characterized by variations of intrapolyhedral bond angles O–M–O (M = W, Zr), with very limited changes in M–O bond lengths and long-range Zr···W distances, achieved though combined librational and translational motions of WO_4 units. Above ~60 K, oscillations appear in experimental data, while the present calculations predict a smooth evolution of the of the Grüneisen parameter. These oscillations were ascribed by Ernst *et al*. to small systematic errors in their lattice-parameter measurements.[18] Such fluctuations in lattice-parameter data might occur as the result of thermally-induced defect creation, as discussed above. As shown in Figure 9, the overall thermal expansion become positive ca. 92 and 131 K below the computed PBEsol and PBE Debye temperature thresholds of 337 and 341 K, respectively, which correspond to the temperature above which most vibrational modes of the crystal are fully excited.[2]

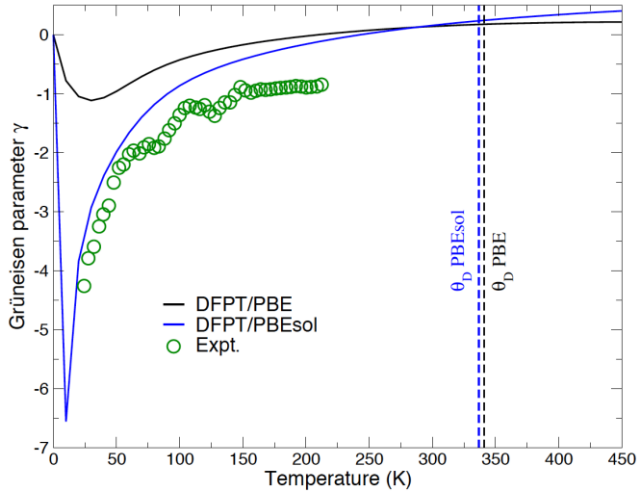

Figure 9. Thermal evolution of the Grüneisen parameter γ of α-ZrW_2O_8 calculated using density functional perturbation theory (DFPT) at the GGA/PBE (solid black line) and GGA/PBEsol (solid blue line) levels within the quasi-harmonic approximation. The experimentally derived Grüneisen parameter (green circles) [Ref. (18)] and the Debye temperatures (θ_D) calculated with PBE and PBEsol (dashed lines) are also displayed.

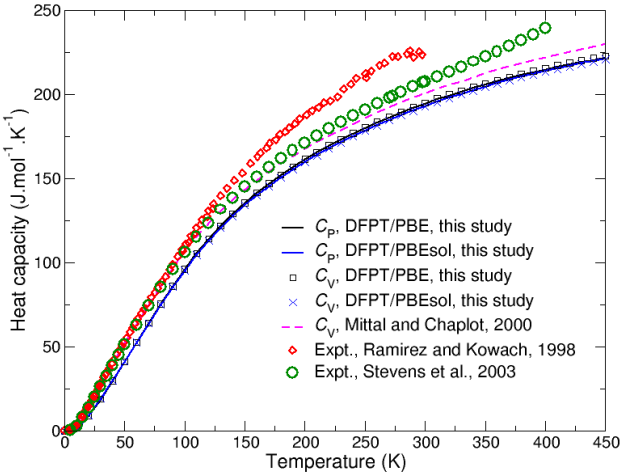

Figure 10. Thermal evolution of the molar isochoric (C_V) and isobaric (C_P) heat capacities of α-ZrW_2O_8 calculated at constant atmospheric pressure using density functional perturbation theory (DFPT) at the GGA/PBE and GGA/PBEsol levels within the quasi-harmonic approximation. Results from lattice dynamics calculations based on semiempirical interaction potentials by Mittal and Chaplot [Ref. (30)] and calorimetric data by Ramirez and Kowach [Ref. (21)] and Stevens et al. [Ref. (29)] are also displayed.

Thermodynamic functions fitted to the Vinet EoS were further derived from phonon calculations. Since α-ZrW_2O_8 is a semiconductor with a calculated band gap of 3.44 and 3.45 eV at the PBE and PBEsol levels, the electronic contribution to the thermodynamic properties is zero and only lattice vibrations contribute to thermodynamic properties. The molar isobaric heat capacity, C_P, as a function of temperature was obtained within the QHA using the expression:

$$C_P(T,P) = -T\frac{\partial^2 G(T,P)}{\partial T^2} = T\frac{\partial V(T,P)}{\partial T}\left.\frac{\partial S(T;V)}{\partial V}\right|_{V=V(T,P)} + C_V[T,V(T,P)], \quad (8)$$

with the molar entropy, S, given by

$$S = -k_B\sum_{\mathbf{q},\nu}\ln\left[1-e^{-\beta\hbar\omega_{\mathbf{q},\nu}}\right] - \frac{1}{T}\sum_{\mathbf{q},\nu}\frac{\hbar\omega_{\mathbf{q},\nu}}{e^{\beta\hbar\omega_{\mathbf{q},\nu}}-1}, \quad (9)$$

the molar isochoric heat capacity, C_V, defined as

$$C_V = k_B\sum_{\mathbf{q},\nu}\left(\beta\hbar\omega_{\mathbf{q},\nu}\right)^2\frac{e^{\beta\hbar\omega_{\mathbf{q},\nu}}}{\left[e^{\beta\hbar\omega_{\mathbf{q},\nu}}-1\right]^2}, \quad (10)$$

where $V(T,P)$ in Eq. (8) is the equilibrium volume at T and P, and the pressure is set to P = 1 bar, *i.e.* the reference ambient pressure for the standard state adopted in calorimetric data; other variables have been defined in Eq. (1).

The thermal evolution of C_P for α-ZrW_2O_8 calculated at constant atmospheric pressure using DFPT at the PBE and PBEsol levels within the QHA is depicted in Figure 10, along with C_P results from lattice dynamics calculations based on semiempirical interaction potentials by Mittal and Chaplot[30] and calorimetric data by Ramirez and Kowach[21] and Stevens et al.[29]. As shown in Figure 10, computed molar isochoric and isobaric heat capacities are similar, with only minute differences between PBE and PBEsol results. At $T = 298.15$ K, the standard molar heat capacity is predicted to be $C_P^0 = 193.8$ and 192.2 J.mol^{-1}.K^{-1} with PBE and PBEsol, respectively, *i.e.*, ~6-7% lower than the value of $C_P^0 = 207.01 \pm 0.21$ J.mol^{-1}.K^{-1} measured by Stevens et al.[29] and ~13-14% smaller than the value of C_P^0~223.3 J.mol^{-1}.K^{-1} reported by Ramirez and Kowach[21]. As discussed by Stevens et al.[29], the results from Ramirez and Kowach[21] are consistently larger than all other sets of calorimetric data,[22,29] due in part to limitations of the relaxation technique utilized at high temperatures, where radiation losses become significant. However, the present results are in closer agreement with the lattice dynamics estimate of C_P^0~199.8 J.mol^{-1}.K^{-1} calculated by Mittal and Chaplot[30] using semiempirical interaction potentials with Born-Mayer type short-range terms and van der Waals type attractive interaction. The agreement between PBE/PBEsol DFPT predictions and semiempirical simulations remains within 3-4% up to the thermal limit of ~431 K corresponding to the $\alpha \rightarrow \beta$ structural phase transition. The value of C_P~219 J.mol^{-1}.K^{-1} obtained with PBE/PBEsol DFPT near this thermal stability limit for α-ZrW_2O_8 is still ~20% smaller than the theoretical Dulong-Petit asymptotic value of $C_P = 3n\mathrm{R} = 274.4$ J.mol^{-1}.K^{-1}, where n is the number of atoms per formula unit and R = 8.314 J.mol^{-1}.K^{-1} is the universal gas constant.

The thermal dependence of the molar entropy of α-ZrW_2O_8 calculated at equilibrium volume with Eq. (9) using DFPT is represented in Figure 11. PBE and PBEsol results are essentially indistinguishable, with standard molar entropy values of S^0~230.3 and 229.2 J.mol^{-1}.K^{-1}, respectively. These values are ~11% smaller than the estimate of $S^0 = 257.96 \pm 0.50$ J.mol^{-1}.K^{-1} obtained by Stevens et al.[29] by integration of their measured molar isobaric heat capacity. The computed thermal evolution of the entropy exhibits a characteristic logarithmically increase according to Boltzmann's entropy formula, $S = k_B.\log(W)$, where W is the number of microstates in the system.

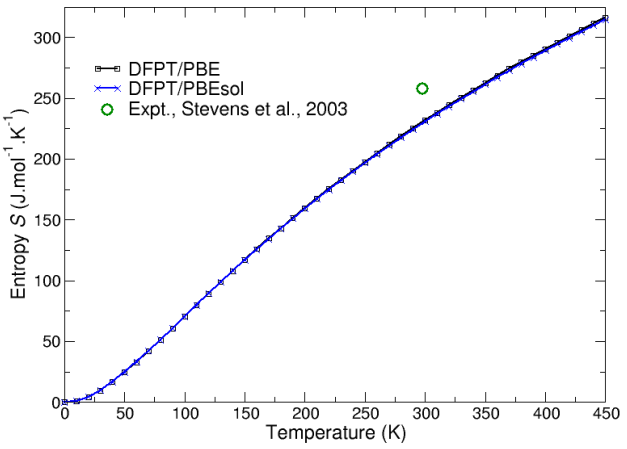

Figure 11. Thermal evolution of the molar entropy of α-ZrW_2O_8 calculated at equilibrium volume using density functional perturbation theory (DFPT) at the GGA/PBE (solid black line) and GGA/PBEsol (solid blue line) levels. The standard molar entropy measured by Stevens et al. [Ref. (29)] is also represented.

4. CONCLUSION

In summary, DFPT calculations were conducted at the GGA/PBE and GGA/PBEsol levels of theory to systematically investigate the crystal structure, phonon, IR and Raman spectra, and thermomechanical properties of the NTE material α-ZrW_2O_8. The accuracy of the DFPT methodology was extensively assessed and validated by performing a comprehensive comparison between results from these calculations and experimental data generated in this study and previous investigations.

Relaxed crystal unit-cell parameters of a = 9.24 and 9.31 Å were obtained at T = 0 K with PBEsol and PBE, respectively, *i.e.*, ~0.6% and ~1.4% larger than the value of 9.1823(4) Å measured by Evans et al. at T = 0.3 K, and ~1.0% and ~1.8% larger than the present XRD estimate of 9.1493(2) Å at room temperature. The accuracy of the PBEsol XC functional in reproducing experimental crystallographic parameters is superior compared to the standard PBE and hybrid B3LYP functionals

In addition, good agreement was obtained between the phonon density of states spectra simulated with DFPT in the athermal limit and the generalized PDOS spectrum from inelastic neutron scattering data collected at T = 300 K using time-of-flight and filter-analyser spectroscopy to probe the low and high phonon-energy range. The only notable exception was for phonon signatures observed in the vicinity of $\omega \cong 600$ cm^{-1}, which are not reproduced by DFPT calculations. Phonon frequencies calculated with PBEsol appear systematically blueshifted compared to PBE results, with larger differences occurring above $\omega \cong 350$ cm^{-1}.

A full assignment of the 55 phonons of α-ZrW_2O_8 was reported based on PBE/PBEsol DFPT calculations and eigenfrequencies predicted with DFPT were systematically compared to IR and Raman bands observed in this study and in previous experiments by Evans et al. and Ravindran et al. From the direct correspondence between the internal modes of WO_4 units in the α-ZrW_2O_8 crystal and a free tungstate ion, PBEsol (PBE) calculations predicted symmetric ν_1 stretching modes in the range 1013−1032 cm^{-1} (993−1012 cm^{-1}), antisymmetric ν_3 stretching modes in the range 739−992 cm^{-1} (717−975 cm^{-1}), antisymmetric ν_4 and symmetric ν_2 bending modes in the range 277−381 cm^{-1} (276−374 cm^{-1}), and a combination of libration, lattice and translation modes below 256 cm^{-1} (253 cm^{-1}). Large gaps of 358 cm^{-1} and 343 cm^{-1} computed with PBEsol and PBE, respectively, separate the high-frequency stretching modes from the low-frequency bending modes, although spectral signatures were previously observed in this range in the generalized PDOS spectrum from inelastic neutron scattering.

Phonon calculations near equilibrium were also carried out within the QHA to derive the thermomechanical properties of α-ZrW_2O_8. At T = 0 K, the bulk modulus values computed using the Vinet EoS are K_0 = 90.2 and 96.7 GPa with the PBE and PBEsol functionals, respectively, in agreement with the experimental value of 104.3 GPa obtained by resonant-ultrasound spectroscopy. These values are consistent with the VRH estimates of 98.7 GPa for PBE and 105.7 GPa for PBEsol derived from the elastic constants calculated with DFPT. In addition, the variation of the linear CTE predicted with PBE/PBEsol DFPT was compared to experimental estimates extracted from the high-resolution neutron diffraction data of David *et al*. between 2 and 520 K. The NTE computed using PBEsol is in very good agreement with experimental data up to ~70 K, where it reaches an extremum of -7.7×10^{-6} K^{-1}. Predictions using PBE are qualitatively similar to PBEsol, although the maximum NTE value predicted is only -4.2×10^{-6} K^{-1} at ~70 K. Above this temperature, both PBEsol and PBE results exhibit smaller NTE values and feature positive thermal expansion above 209 K and 243 K, respectively. While reduction in NTE also appears above ~70 K in the experimental data for polycrystalline ZrW_2O_8, computational predictions for single crystal α-ZrW_2O_8 differ from measurements, which oscillate between -10.8×10^{-6} K^{-1} and -8.4×10^{-6} K^{-1} in the temperature range ~70−300 K. Such differences might stem from the creation of thermally induced defects in α-ZrW_2O_8 samples, as precursors to the thermally activated $\alpha \rightarrow \beta$ phase transition in cubic ZrW_2O_8, which occurs around 431 K. The thermal evolution of the Grüneisen parameter γ predicted with PBEsol is in excellent agreement with experimental estimates by Ernst and co-workers to ~60 K, while PBE predictions systematically underestimate experimental data. Calculations at the PBEsol and PBE levels indicate that γ is negative below 245 and 210 K, respectively, with minima of -6.56 at 10 K for PBEsol and -1.11 at 30 K for PBE. The main contributions to NTE at low temperature stem from the two lowest-frequency optical phonons, predicted at 36 cm^{-1} (T irrep) and 37 cm^{-1} (E irrep) with PBEsol and at 39 and 42 cm^{-1} with PBE.

Finally, the thermal evolutions of the molar isochoric and isobaric heat capacities and molar entropy were calculated for single-crystal α-ZrW_2O_8 using DFPT at the PBE and PBEsol levels. At $T = 298.15$ K, the standard molar heat capacity is predicted to be $C_P^0 = 193.8$ and 192.2 J.mol^{-1}.K^{-1} with PBE and PBEsol, respectively, *i.e.*, ~6-7% lower than the value of $C_P^0 = 207.01 \pm 0.21$ J.mol^{-1}.K^{-1} measured by Stevens et al. and ~13-14% smaller than the value of $C_P^0 \sim 223.3$ J.mol^{-1}.K^{-1} reported by Ramirez and Kowach. However, the present results are in closer agreement with the lattice dynamics estimate of $C_P^0 \sim 199.8$ J.mol^{-1}.K^{-1} calculated by Mittal and Chaplot using semiempirical interaction potentials. PBE and PBEsol results for the entropy are essentially identical, with standard molar entropy values of $S^0 \sim 230.3$ and 229.2 J.mol^{-1}.K^{-1}, respectively. These values are ~11% smaller than the estimate of $S^0 = 257.96 \pm 0.50$ J.mol^{-1}.K^{-1} obtained by Stevens et al. by integration of their measured molar isobaric heat capacity.

The present results and finding demonstrate the accuracy of the DFPT/PBEsol approach for studying the spectroscopic, mechanical

and thermodynamic properties of stoichiometric materials with anomalous thermal expansion. Further DFPT investigations will focus on the role of defects and impurities in NTE materials, since a full understanding of the structure-properties relationship is still currently missing for this class of systems.

ASSOCIATED CONTENT

Supporting Information

Experimental details of the precipitation of the cubic hydrated precursor $ZrW_2O_7(OH)_2(H_2O)_2$ and conversion to the final α-ZrW_2O_8 phase are given in Supporting Information, along with and SEM and XRD characterization of these compounds. Computational methods utilized to obtain elastic constants and derive shear and Young's moduli, Poisson's ratio, and Debye temperature are also discussed in Supporting Information.

AUTHOR INFORMATION

Corresponding Author

*E-mail pfweck@sandia.gov; Ph 505-844-8144 (P.F.W.).

ORCID

Philippe F. Weck: 0000-0002-7610-2893

Notes

The authors declare no competing financial interests.

ACKNOWLEDGMENT

Sandia National Laboratories is a multi-mission laboratory managed and operated by National Technology and Engineering Solutions of Sandia, LLC., a wholly owned subsidiary of Honeywell International, Inc., for the U.S. Department of Energy's National Nuclear Security Administration under Contract DE-NA0003525. This work was supported by Laboratory Directed Research and Development (LDRD) funding from Sandia National Laboratories.

REFERENCES

[1] Kittel, C. *Introduction to Solid State Physics*, 7th ed., Wiley, New York, 1996.

[2] Chu, C. N.; Saka, N.; Suh, N. P. Negative Thermal Expansion Ceramics: A Review. *Mater. Sci. Eng*. **1987**, *95*, 303–308.

[3] Roy, R.; Agrawal, D. K.; McKinstry, H. A. Very Low Thermal Expansion Coefficient Materials. *Ann. Rev. Matter. Sci*. **1989**, *19*, 59–81.

[4] White, G. K. Solids: Thermal Expansion and Contraction. *Contemp. Phys*. **1993**, *34*, 193.

[5] Sleight, A. W. Isotropic Negative Thermal Expansion. *Ann. Rev. Matter. Sci.* **1998**, *28*, 29–43.

[6] Evans, J. S. O. Negative Thermal Expansion Materials. *J. Chem. Soc. Dalton Trans.* **1999**, 3317–3326.

[7] Barrera, G. D.; Bruno, J. A. O.; Barron, T. H. K.; Allan, N. L. Negative Thermal Expansion. *J. Phys.: Condens. Matter* **2005**, *17*, R217.

[8] Takenaka, K. Negative Thermal Expansion Materials: Technological Key for Control of Thermal Expansion. *Sci. Technol. Adv. Mater*. **2012**, *13*, 013001.

[9] Lind, C. Two Decades of Negative Thermal Expansion Research: Where Do We Stand? *Materials* **2012**, *5*, 1125– 1154.

[10] Dove, M. T.; Fang, H. Negative Thermal Expansion and Associated Anomalous Physical Properties: Review of the Lattice Dynamics Theoretical Foundation. *Rep. Prog. Phys.* **2016**, *79*, 066503.

[11] Graham, J.; Wadsley, A. D., Weymouth, J. H.; Williams, L. S. A new ternary oxide, ZrW_2O_8. *J. Am. Ceram. Soc*. **1959**, *42*, 570.

[12] Martinek, C.; Hummel, F.A. Linear Thermal Expansion of Three Tungstates. *J. Am. Ceram. Soc.* **1968**, *51*, 227–228.

[13] Auray, M.; Quarton, M.; Leblanc, M. Zirconium Tungstate. *Acta Crystallogr. C* **1995**, *51*, 2210-2213.

[14] Mary, T. A.; Evans, J. S. O.; Sleight, A. W.; Vogt, T. Negative Thermal Expansion from 0.3 to 1050 Kelvin in ZrW_2O_8. *Science* **1996**, *272*, 90-92.

[15] Evans, J. S. O.; Mary, T. A.; Vogt, T.; Subramanian, M. A.; Sleight, A. W. Negative Thermal Expansion in ZrW_2O_8 and HfW_2O_8. *Chem. Mater*. **1996**, *8*, 2809-2823.

[16] Evans, J. S. O.; Hu, Z.; Jorgensen, J. D.; Argyriou, D. N.; Short, S.; Sleight, A. W. Compressibility, Phase Transitions, and Oxygen Migration in Zirconium Tungstate, ZrW_2O_8. *Science* **1997**, *275*, 61-65.

[17] Evans, J. S. O.; David, W. I. F., Sleight, A. W. Structural Investigation of the Negative-Thermal-Expansion Material ZrW_2O_8. *Acta Crystallogr.B* **1999**, *55*, 333-340.

[18] Ernst, G.; Broholm, C.; Kowach, G. R.; Ramirez, A. P. Phonon density of states and negative thermal expansion in ZrW_2O_8. *Nature* **1998**, *396*, 147-149.

[19] David, W. I. F.; Evans, J. S. O.; Sleight, A. W. Direct Evidence for a Low-Frequency Phonon Mode Mechanism in the Negative Thermal Expansion Compound ZrW_2O_8. *Europhys. Lett.* **1999**, *46*, 661-666.

[20] Perottoni, C.A.; da Jornada, J.A.H. Pressure-Induced Amorphization and Negative Thermal Expansion in ZrW_2O_8. *Science* **1998**, *280*, 886-889.

[21] Ramirez, A. P.; Kowach, G. Large Low Temperature Specific Heat in the Negative Thermal Expansion Compound ZrW_2O_8. *Phys. Rev. Lett.* **1998**, *80*, 4903-4906.

[22] Yamamura, Y.; Nakajima, N.; Tsuji, T. Heat Capacity Anomaly Due to the α to β Structural Phase Transition in ZrW_2O_8. *Solid. State Commun*. **2000**, *114*, 453–455.

[23] Ravindran, T. R.; Arora, A. K.; Mary, T. A. High Pressure Behavior of ZrW_2O_8: Grüneisen Parameter and Thermal Properties. *Phys. Rev. Lett.* **2000**, *84*, 3879.

[24] Ravindran, T. R.; Arora, A. K.; Mary, T. A. High-Pressure Raman Spectroscopic Study of Zirconium Tungstate. *J. Phys: Condens. Matter* **2001**, *13*, 11573-11588.

[25] Drymiotis, F. R.; Ledbetter, H.; Betts, J. B.; Kimura, T.; Lashley, J. C., Migliori, A.; Ramirez, A.; Kowach, G.; Van Dujin, J. Monocrystal Elastic Constants of the Negative-Thermal-Expansion Compound Zirconium Tungstate (ZrW_2O_8). *Phys. Rev. Lett.* **2004**, *93*, 025502.

[26] Jason N. Hancock, Chandra Turpen, and Zack Schlesinger, Glen R. Kowach, Arthur P. Ramirez. *Phys. Rev. Lett*. **2004**, *93*, 225501.

[27] Keen, D. A.; Goodwin, A. L.; Tucker, M. G.; Dove, M. T.; Evans, J. S. O.; Crichton, W. A.; Brunelli, M. Structural Description of Pressure-Induced Amorphization in ZrW_2O_8. *Phys. Rev. Lett*. **2007**, *98*, 225501.

[28] Bridges, F.; Keiber, T.; Juhas, P.; Billinge, S. J. L.; Sutton, L.; Wilde, J.; Kowach, G. R. Local Vibrations and Negative Thermal Expansion in ZrW_2O_8. *Phys. Rev. Lett*. **2014**, *112*, 045505.

[29] Stevens, R.; Linford, J.; Woodfield, B. F.; Boerio-Goates, J.; Lind, C.; Wilkinson, A. P.; Kowach, G. Heat Capacities, Third-Law Entropies and Thermodynamic Functions of the Negative Thermal Expansion Materials, Cubic a-ZrW_2O_8 and Cubic $ZrMo_2O_8$, From T = (0 to 400 K). *J. Chem. Thermo*. **2003**, *35*, 919–937.

[30] Mittal, R.; Chaplot, S. L. Phonon Density of States and Thermodynamic Properties in Cubic and Orthorhombic Phases of ZrW_2O_8. *Solid State Communications* **2000**, *115*, 319–322.

[31] Sanson, A. Toward an Understanding of the Local Origin of Negative Thermal Expansion in ZrW_2O_8: Limits and Inconsistencies of the Tent and Rigid Unit Mode Models. *Chem. Mater*. **2014**, *26*, 3716-3720.

[32] Ramzan, M.; Luo, W.; Ahuja, R. High Pressure, Mechanical, and Optical Properties of ZrW_2O_8. *J. Appl. Phys*. **2011**, *109*, 033510.

[33] Gava, V.; Martinotto, A. L.; Perottoni, C. A. First-Principles Mode Grüneisen Parameters and Negative Thermal Expansion in α-ZrW_2O_8. *Phys. Rev. Lett*. **2012**, *109*, 195503.
[34] Gupta, M. K.; Mittal, R.; Chaplot, S. L Negative Thermal Expansion in Cubic ZrW_2O_8: Role of Phonons in the Entire Brillouin Zone from Ab Initio Calculations. *Phys. Rev. B* **2013**, *88*, 014303.
[35] Perdew, J. P.; Burke, K.; Ernzerhof, M. Generalized Gradient Approximation Made Simple. *Phys. Rev. Lett*. **1996**, *77*, 3865-3868.
[36] Perdew, J. P.; Ruzsinszky, A.; Csonka, G. I.; Vydrov, O. A.; Scuseria, G. E.; Constantin, L. A.; Zhou, X.; Burke, K. Restoring the Density-Gradient Expansion for Exchange in Solids and Surfaces. *Phys. Rev. Lett.* **2008**, *100*, 136406-.
[37] Gonze, X.; Lee, C. Dynamical matrices, Born effective charges, dielectric permittivity tensors, and interatomic force constants from density-functional perturbation theory. *Phys. Rev. B* **1997**, *55*, 10355.
[38] Weck, P. F.; Kim, E. Assessing Hubbard-Corrected AM05+U and PBEsol+U Density Functionals for Strongly Correlated Oxides CeO_2 and Ce_2O_3. *Chem. Phys. Phys. Chem*. **2016**, *18*, 26816-26826.
[39] Weck, P. F.; Kim, E. Uncloaking the Thermodynamics of the Studtite to Metastudtite Shear-Induced Transformation. *J. Phys. Chem. C* **2016**, *120*, 16553-16560.
[40] Weck, P. F.; Kim, E.; Tikare, V.; Mitchell, J. A. Mechanical Properties of Zirconium Alloys and Zirconium Hydrides Predicted from Density Functional Perturbation Theory. *Dalton Trans*. **2015**, *44*, 18769-18779.
[41] Johnson, T. J.; Sweet, L. E.; Meier, D. E.; Mausolf, E. J.; Kim, E.; Weck, P. F.; Buck, E. C.; McNamara, B. K. Time-Resolved Infrared Reflectance Studies of the Dehydration-Induced Transformation of Uranyl Nitrate Hexahydrate to the Trihydrate Form. *J. Phys. Chem. A* **2015**, *119*, 9996-10006.
[42] Weck, P. F.; Kim E. Layered uranium(VI) hydroxides: structural and thermodynamic properties of dehydrated schoepite α-$UO_2(OH)_2$. *Dalton Trans.* **2014**, *43*, 17191.
[43] Weck, P. F.; Kim E. Solar Energy Storage in Phase Change Materials: First-Principles Thermodynamic Modeling of Magnesium Chloride Hydrates. *J. Phys. Chem. C* **2014**, *118*, 4618.
[44] Kresse, G.; Furthmüller, J. Efficient Iterative Schemes for Ab Initio Total-Energy Calculations Using a Plane-Wave Basis Set. *Phys. Rev.* B **1996**, *54*, 11169-11186.
[45] Weck, P. F.; Juan, P.-A.; Dingreville, R.; Kim, E. Density Functional Analysis of Fluorite-Structured $(Ce,Zr)O_2/CeO_2$ Interfaces. *J. Phys. Chem. C* **2017**, *121*, 14678.
[46] Colmenero, F.; Bonales, L. J.; Cobos, J.; Timon, V. Density Functional Theory Study of the Thermodynamic and Raman Vibrational Properties of gamma-UO_3 Polymorph. *J. Phys. Chem. C* **2017**, *121*, 14507–14516.
[47] Blöchl, P. E. Projector Augmented-Wave Method. *Phys. Rev.* B **1994**, *50*, 17953-17979.
[48] Kresse, G.; Joubert, D. From Ultrasoft Pseudopotentials to the Projector Augmented-Wave Method. *Phys. Rev.* B **1999**, *59*, 1758-1775.
[49] Davidson, E. R. *Methods in Computational Molecular Physics*, G. H. F. Diercksen and S. Wilson, Eds., Vol. 113, NATO Advanced Study Institute, Series C, Plenum, New York, 1983, p. 95.
[50] Monkhorst, H. J.; Pack, J. D. Special Points for Brillouin-Zone Integrations. *Phys. Rev.* B **1976**, *13*, 5188-5192.
[51] Togo, A.; Oba, F.; Tanaka, I. First-Principles Calculations of the Ferroelastic Transition Between Rutile-Type and $CaCl_2$-Type SiO_2 at High Pressures. *Phys. Rev.* B **2008**, *78*, 134106.
[52] Colmenero, F.; Bonales, L.J.; Cobos, J.; Timon, V. Thermodynamic and Mechanical Properties of the Rutherfordine Mineral Based on Density Functional Theory. *J. Phys. Chem. C* **2017**, *121*, 5994-6001.
[53] Weck, P. F.; Kim, E.; Buck, E. C. On the Mechanical Stability of Uranyl Peroxide Hydrates: Implications for Nuclear Fuel Degradation. *RSC Adv*. **2015**, *5*, 79090-79097.
[54] Weck, P. F.; Kim, E.; Jove-Colon, C. F. Relationship Between Crystal Structure and Thermo-Mechanical Properties of Kaolinite Clay: Beyond Standard Density Functional Theory. *Dalton Trans*. **2015**, *44*, 12550-12560.
[55] Weck, P. F.; Kim, E. Thermodynamics of Technetium: Reconciling Theory and Experiment Using Density Functional Perturbation Analysis. *Dalton Trans*. **2015**, *44*, 12735-12742.
[56] Closmann, C.; Sleight, A. W.; Haygarth, J. C. Low-Temperature Synthesis of ZrW_2O_8 and Mo-Substituted ZrW_2O_8. *J. Sol. State Chem*. **1998**, *139*, 424-426.
[57] Dresselhaus, M. S.; Dresselhaus, G.; Jorio, A. *Group Theory: Application to the Physics of Condensed Matter*, Springer-Verlag, Berlin, 2008, p. 479.
[58] Turel, G. *Infrared and Raman Spectra of Crystals*, Academic Press, New York, 1972.
[59] Herzberg, G. *Molecular Spectra and Molecular Structure. Vol.2: Infrared and Raman Spectra of Polyatomic Molecules*, Van Nostrand-Reinhold, New York, 1962.
[60] Phillippi, C. M.; Mazdiyasni, K. S. Infrared and Raman Spectra of Zirconia Polymorphs. *J. Am. Ceram. Soc*. **1971**, *54*, 254-258.
[61] Gabrusenoks, J.; Veispals, A.; von Czarnowski, A.; Meiwes-Broer, K.-H. Infrared and Raman Spectroscopy of WO_3 and $CdWO_4$. Electrochimica Acta **2001**, *46*, 2229-2231.
[62] Chang, L.L.Y.; Scroger, M. G.; Phillips, B. Condensed Phase Relations in Systems ZrO_2-WO_2-WO_3 and HfO_2-WO_2-WO_3. *J. Am. Ceram. Soc.* **1967**, *50*, 211.
[63] P. Vinet, J. R. Rose, J. Ferrante, J. R. Smith, *J. Phys.: Condens. Matter*, 1989, **1**, 1941.
[64] Born, M. On the Stability of Crystal Lattices. I. *Math. Proc. Cambridge Philos. Soc.* **1940**, *36*, 160-172.
[65] Born, M.; Huang, K. *Dynamics Theory of Crystal Lattices*, Oxford University Press, Oxford, 1954.
[66] Wachtman, J. B. Jr; Tefft, W.E.; Lam, D. G. Jr.; Apstein, C. S. Exponential Temperature Dependence of Young's Modulus for Several Oxides. *Phys. Rev*. **1961**, *122*, 1754.
[67] Grüneisen, E. Theory of the Solid State of Monoatomic Elements. *Ann. Phys*. **1912**, *39*, 257-306.
[68] Grüneisen, E. Zustand des Festen Koerpers. *Handbuch Phys*. **1926**, *10*, 1-52.